INORGANIC CHEMISTRY
FRONTIERS

RESEARCH ARTICLE

View Article Online
View Journal | View Issue

Cite this: *Inorg. Chem. Front.*, 2026, **13**, 86

Improper narrow bandgap molecular ferroelectrics enable light-excited pyroelectricity for broadband self-powered photoactivities

Jialu Chen,[a,b] Liwei Tang,[a] Chen Gong,[a] Linjie Wei,[a] Jingtian Zhang,[a] Xingguang Chen,[a] Xiaoyu Zhang,[a,b] Yi Liu,*[a,c] Junhua Luo [a,c] and Zhihua Sun *[a,c]

Narrow bandgap ferroelectrics are emerging as critical components for assembling high-performance optoelectronic devices with a broadband spectral response, yet integrating narrow bandgap and robust ferroelectricity in a single-phase material system remains a huge challenge. Herein, we report a narrow bandgap improper molecular ferroelectric, (DMAPA)BiI_5 (**1**; DMAPA = dimethylaminopropyl ammonium), which has a bandgap of 1.94 eV and a spontaneous polarization (P_s) value of 1.38 μC cm^{-2}. It is notable that **1** exhibits unusual dielectric bistability near its Curie temperature (T_c) = 372 K, along with only quite small variation in dielectric constants. This characteristic of improper ferroelectricity endows **1** with large pyroelectric figures-of-merit. Strikingly, light-induced change of its electric P_s leads to ultraviolet-to-near-infrared pyroelectricity in a wide spectral region (266–980 nm), thus achieving broadband self-powered photoactivities. High-quality thin films of **1** fabricated *via* a spin-coating process also exhibit excellent light-induced pyroelectric effects. The integration of photoactivities in narrow bandgap improper ferroelectrics offers a promising pathway toward scalable broadband optoelectronic device application.

Received 28th August 2025,
Accepted 16th October 2025

DOI: 10.1039/d5qi01797a

rsc.li/frontiers-inorganic

Introduction

Ferroelectrics have been developed as an indispensable class of electroactive materials, which are characterized by reversible switching of spontaneous polarization (P_s) under external electric fields.[1–3] The inherent absence of inversion symmetry in ferroelectrics gives rise to a series of coupled physical properties, including pyroelectricity, piezoelectricity, and optical nonlinearity.[4,5] These multifunctional properties have a wide range of high-performance electronic and optoelectronic applications, such as piezoelectric sensors, switchable diodes, and self-powered photodetectors.[6,7] In normal ferroelectrics, P_s serves as the primary order parameter during phase transitions. Conversely, for improper ferroelectrics, P_s acts as a second-order parameter induced by structural distortions, spin ordering, or charge ordering.[8–10] Improper ferroelectrics usually show small variation in dielectric constants near the Curie temperature (T_c), with values consistently at least an order of magnitude lower than those of proper ferroelectrics.[11,12] Dielectric bistability refers to switchable dielectric states, characterized by the presence of two stable phases that remain nearly temperature invariant during phase transitions. The relatively small dielectric constant values may indicate the presence of improper ferroelectricity, thereby enabling dramatic pyroelectric figures-of-merit (FOMs) or light-induced pyroelectricity.[13] Conventional inorganic oxide ferroelectrics such as $PbTiO_3$, $PbZrO_3$, and $NaNbO_3$ typically possess wide bandgaps (3.5–4.1 eV),[14] limiting their ability to harvest solar energy efficiently across the visible and near-infrared (NIR) spectra. Although ferroelectric materials with narrow bandgaps are highly desirable for applications such as broadband photodetection and solar-powered energy harvesting,[15] the associated increase in leakage current often compromises polarization stability and deteriorates ferroelectric performances.[16] Therefore, realizing the coexistence of a narrow bandgap and stable ferroelectricity is a crucial bottleneck in the development of multifunctional optoelectronic materials.

Recently, organic–inorganic hybrid perovskites (OIHPs) have emerged as a versatile platform for the development of new ferroelectric materials with tunable optical and electronic properties.[17,18] OIHPs are formed through chemical self-

[a]*State Key Laboratory of Functional Crystals and Devices, Fujian Institute of Research on the Structure of Matter, Chinese Academy of Sciences, Fuzhou, Fujian 350002, China. E-mail: sunzhihua@fjirsm.ac.cn*
[b]*College of Chemistry and Materials Science, Fujian Normal University, Fuzhou 350007, China*
[c]*Fujian College, University of Chinese Academy of Sciences, Fuzhou 350000, China*

assembly of inorganic metal–halogen frameworks and organic cations.[19] These architectures combine the design flexibility and solution processability of organic molecules with the functional robustness of inorganic networks.[20] Inorganic metal–halide frameworks play a dominant role in determining the energy band structure.[21,22] Thus, the engineering of metal and halide compositions (*e.g.*, Cl, Br, and I) can effectively tailor the band edge positions and optical bandgap.[23,24] Simultaneously, the incorporation of polar organic cations can induce lattice distortions that support ferroelectric behavior, yielding both efficient light absorption and polarization switching capability.[25,26] This unique combination establishes OIHPs as promising optoelectronic candidates, positioning them as cornerstone architectures for new molecular ferroelectric systems.

As the emerging ferroelectric subclass of OIHPs, bismuth (Bi)-based alternatives have attracted increasing attention due to their flexible electronic structures and superior environmental compatibility.[27–37] In this work, we have developed a new Bi-based molecular ferroelectric with a narrow bandgap (~1.94 eV), (DMAPA)BiI_5 (**1**), which exhibits bistable dielectricity and improper ferroelectricity. Strikingly, light-induced pyroelectricity in the ultraviolet (UV)-to-near-infrared (NIR) spectral region achieves broadband self-powered photoactivity. The successful fabrication of high-quality thin films further highlights its potential for scalable integration into advanced optoelectronic systems.

Results and discussion

Variable-temperature structure analyses

High-quality red-black crystals of **1** were obtained by slowly cooling its solution in HI, as depicted in Fig. 1a. The powder X-ray diffraction (XRD) results match well with the simulated pattern, verifying the phase purity of **1** and its phase stability over 120 days (Fig. S1). Thermogravimetric analysis (TGA) indicates that **1** can be thermally stable up to 571 K without any thermal decomposition (Fig. S2). To elucidate structural features and correlate them with functional properties, single-

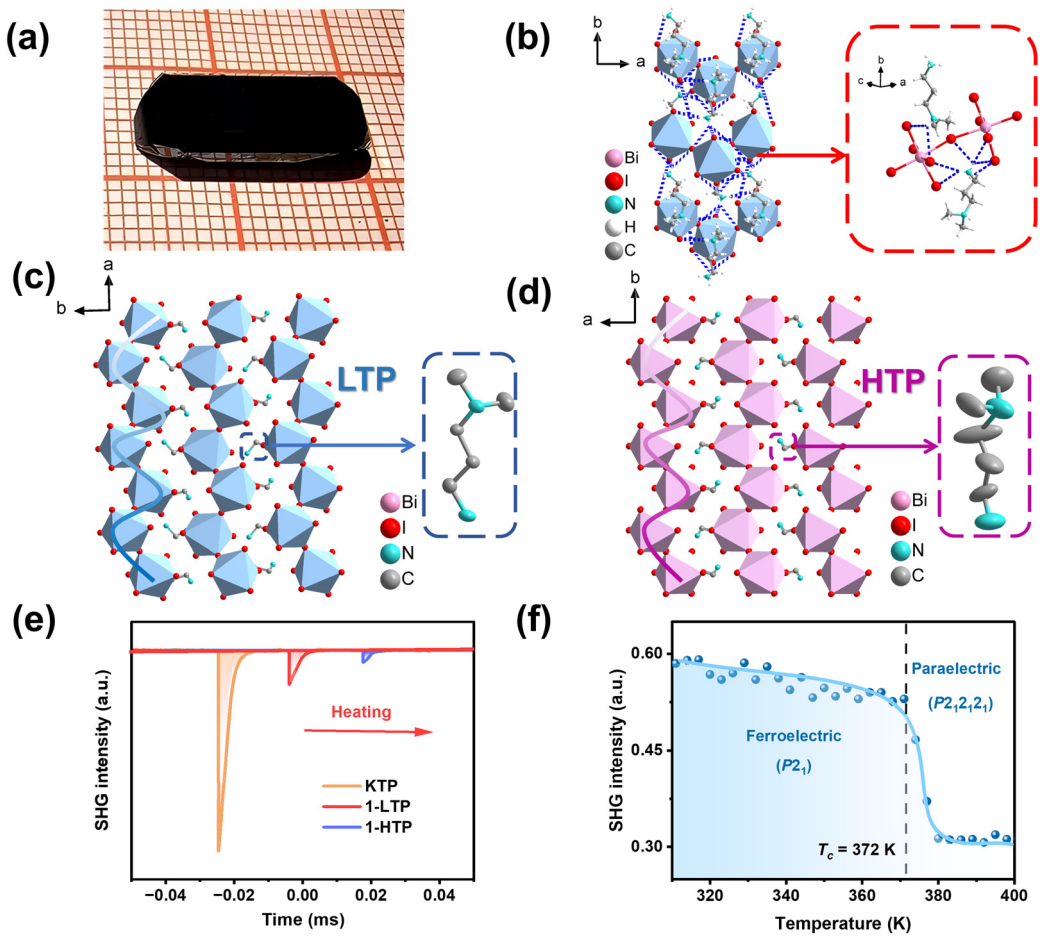

Fig. 1 Crystal structures of **1** at different phases. (a) Bulk crystal obtained by the temperature-cooling method. (b) N–H···I hydrogen-bonding interactions between organic cations and inorganic frameworks at 273 K. (c) Packing diagram as viewed in the direction of the *c*-axis at 273 K (ferroelectric phase, FEP). The small cation configuration at the ferroelectric phase is highlighted within the blue rectangle. (d) Packing structure observed at 400 K (paraelectric phase, PEP). (e) The comparison of SHG signals of **1** and KDP. (f) Variable-temperature SHG intensities.

crystal X-ray diffraction analysis was performed. At 273 K, **1** crystallizes in the monoclinic chiral space group $P2_1$. The basic structure adopts a 1D chain-like topology spiraling along the *a*-axis, composed of organic cations and extended inorganic framework chains formed by the face sharing BiI_6 octahedra (Fig. 1c). Since an ideal octahedron requires uniform bond lengths and angles, **1** exhibits stereochemical geometry distortion characterized by bond length variations (2.961–3.351 Å) and angular deviations (167.25°–171.58°), as quantified in Fig. S3 and Table S3. Each organic $(DMAPA)^{2+}$ cation contributes two fully protonated ammonium groups, with N–H···I hydrogen bonds anchoring the inorganic chains (Fig. 1b).

Two adjacent cations parallel to the *a*-axis exhibit mutual tilting at a specific angle. Structurally, the directional alignment of organic cations combined with BiI_6 octahedral tilting facilitates electric polarization. The high-temperature phase (HTP) of **1** crystallizes in the nonpolar orthorhombic space group $P2_12_12_1$. Organic cations display significantly expanded thermal ellipsoids compared to the low-temperature phase (LTP), indicating an order–disorder transformation (Fig. 1d). Furthermore, variable-temperature second harmonic generation (SHG) served as an effective technique for symmetry breaking across the phase transition (Fig. 1e). At the LTP, the SHG signal exhibits a sharp intensity, approximately 0.2 times that of KH_2PO_4 (KDP), confirming that **1** crystallizes in a noncentrosymmetric space group at room temperature. Upon heating, the SHG signals exhibit an abrupt decrease above T_c, with the intensity reduced to approximately 0.1 times that of KDP (Fig. 1f). This result unambiguously confirms that **1** undergoes a phase transition and that the space group $P2_12_12_1$ is consistent with its noncentrosymmetric structure in the HTP. This process corresponds to the symmetry breaking characterized by the Aizu notation of $222F2$.[1,38] The number of symmetric elements reduces from 4 (E, C_2, $C_{2'}$, $C_{2''}$) to 2 (E, C_2), consistent with Landau phase transition theory (Fig. S4). In this context, the ferroelectric phase transition of **1** represents a temperature-driven order–disorder transition driven by the molecular motion of $(DMAPA)^{2+}$ cations.

Ferroelectric and phase transition properties

The structural changes of **1** are closely correlated with its phase transition behavior, preliminarily confirmed by differential scanning calorimetry (DSC) measurements. As shown in Fig. 2a, a pair of endothermic/exothermic peaks at 372/370 K are clearly observed during heating and cooling processes, indicating a reversible phase transition in **1**. Specific heat capacity (C_p) measurement further corroborates this transition (Fig. S5). Besides, distinct step-like dielectric anomalies are

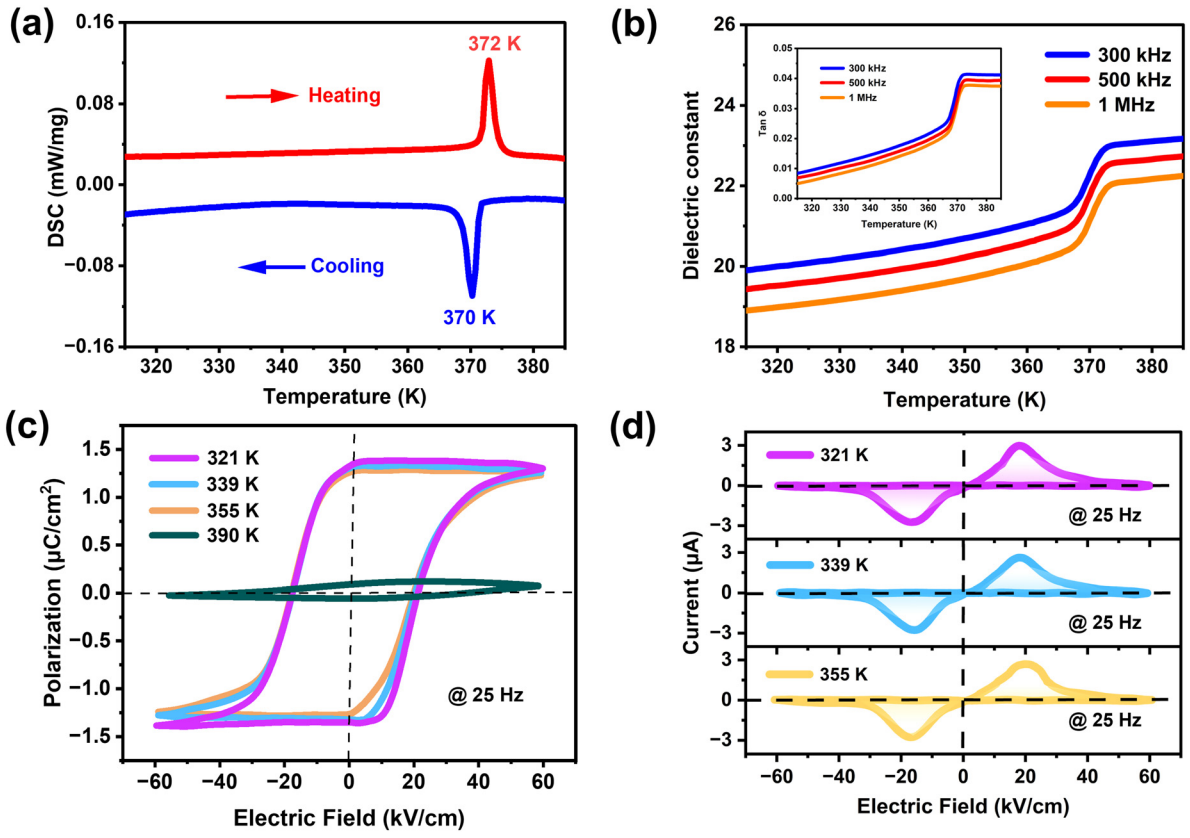

Fig. 2 Structural phase transition and related physical properties of **1**. (a) DSC curves measured upon heating and cooling. (b) Temperature dependence of the dielectric constant. Inset: the corresponding dielectric loss. (c) *P*–*E* hysteresis loops obtained at different temperatures (f = 25 Hz). (d) The current loop of **1** measured at different temperatures (f = 25 Hz).

also observed near to 372 K, as depicted in Fig. 2b. The dielectric constant (ε_r) of **1** exhibits a very small change from 20 to 23 at 300 kHz during the phase transition, and two stable dielectric plateaus are observed upon heating. **1** exhibits minimal dielectric loss ($\tan\delta$) variation from 0.008 to 0.04 at 300 kHz near its T_c (Fig. 2b). The minimal temperature-dependent variations in the dielectric constant and dielectric loss across broad thermal ranges hint at the improper ferroelectric characteristics of **1**.[13,39] Such temperature-dependent properties near the T_c demonstrate dielectric bistability in **1**, where P_s functions as a secondary order parameter of improper ferroelectrics. It is proposed that exploiting dielectric bistability in improper ferroelectrics provides an effective strategy for optimizing pyroelectric FOMs.

The definitive characteristic of ferroelectric materials is the reversible switching of P_s direction under applied external electric fields.[40] This can be verified through polarization–electric field (*P–E*) hysteresis loop measurement. As illustrated in Fig. 2c, the well-defined *P–E* hysteresis loops measured at different temperatures provide solid evidence for the ferroelectricity in **1**. At 321 K, the *P–E* loop gives a P_s value of approximately ~1.4 μC cm^{-2} and a coercive field (E_c) of ~17 kV cm^{-1}, significantly lower than the values for inorganic ferroelectric $BaTiO_3$ (E_c = 30 kV cm^{-1}) and polymer PVDF (E_c = 500 kV cm^{-1}).[41,42] When the temperature exceeds its T_c (372 K), the remanent polarization drops to zero, and **1** transforms to the paraelectric phase. The two opposing current peaks in the current–voltage (*J–E*) curves at various temperatures also serve as conclusive evidence of ferroelectricity in **1** (Fig. 2d).

Band gap calculation theory and comparative analysis

To investigate the optical properties of **1**, the UV-vis absorption spectrum was recorded at room temperature. As shown in Fig. 3a, the spectrum exhibits a strong absorption onset at the band edge (639 nm). By analyzing the power law dependence of the absorption coefficient on photon energy (inset of Fig. 3a), the bandgap was determined to be 1.94 eV. The bandgap value obtained from first-principles band structure calculations is 1.86 eV (Fig. 3b), being consistent with the experimentally determined result. PDOS analysis reveals that the valence band maximum (VBM) and the conduction band minimum (CBM) at the G-point are primarily constituted by I-5p and Bi-6p orbitals (Fig. 3c). This finding underscores the decisive role of the inorganic framework in modulating the bandgap and electronic structure. Notably, the bandgap of **1** remains relatively narrow among known ferroelectrics (Fig. 3d).[43–48] The core advantage of narrow bandgap molecular ferroelectrics lies in their broadened spectral response range, which manifests pronounced light-induced pyroelectric effects *via* synergistic interplay with the ferroelectric polarization field.[49]

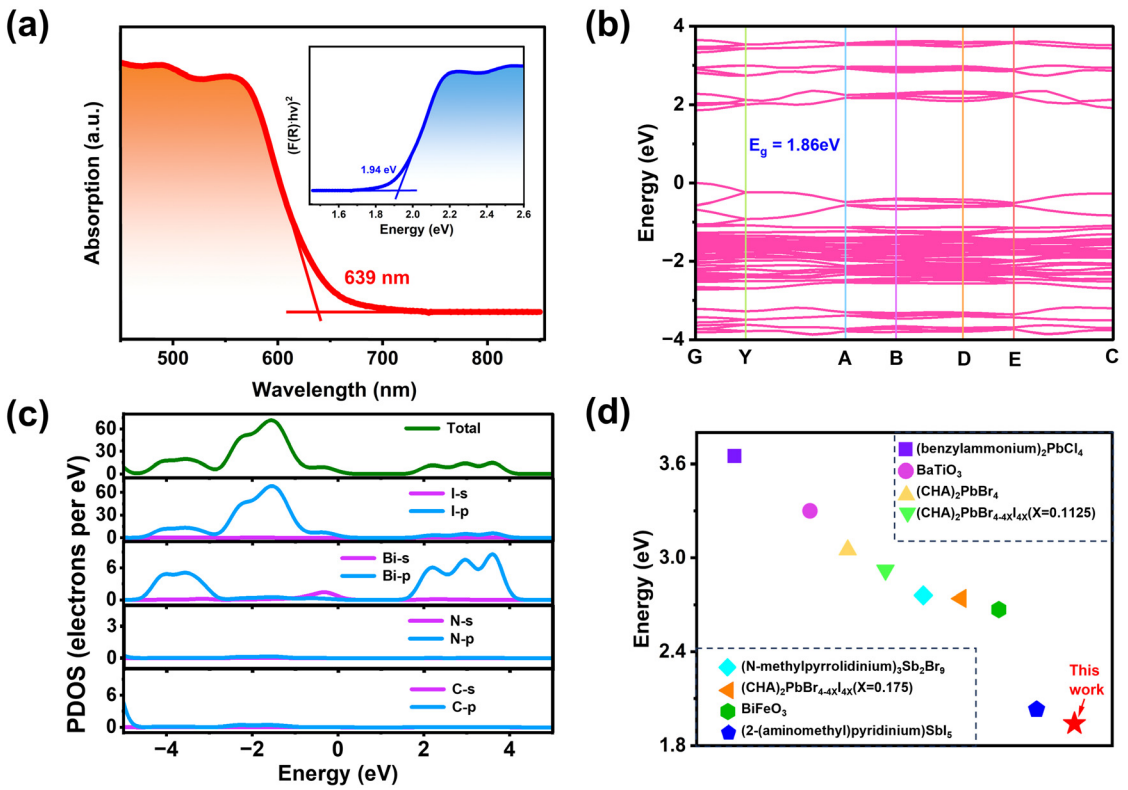

Fig. 3 (a) UV-vis absorption spectra of **1**. Inset: the corresponding *Tauc* plot. (b) Calculated band structure and (c) PDOS spectra near the Fermi level. (d) Bandgap comparison of **1** and several typical ferroelectrics.

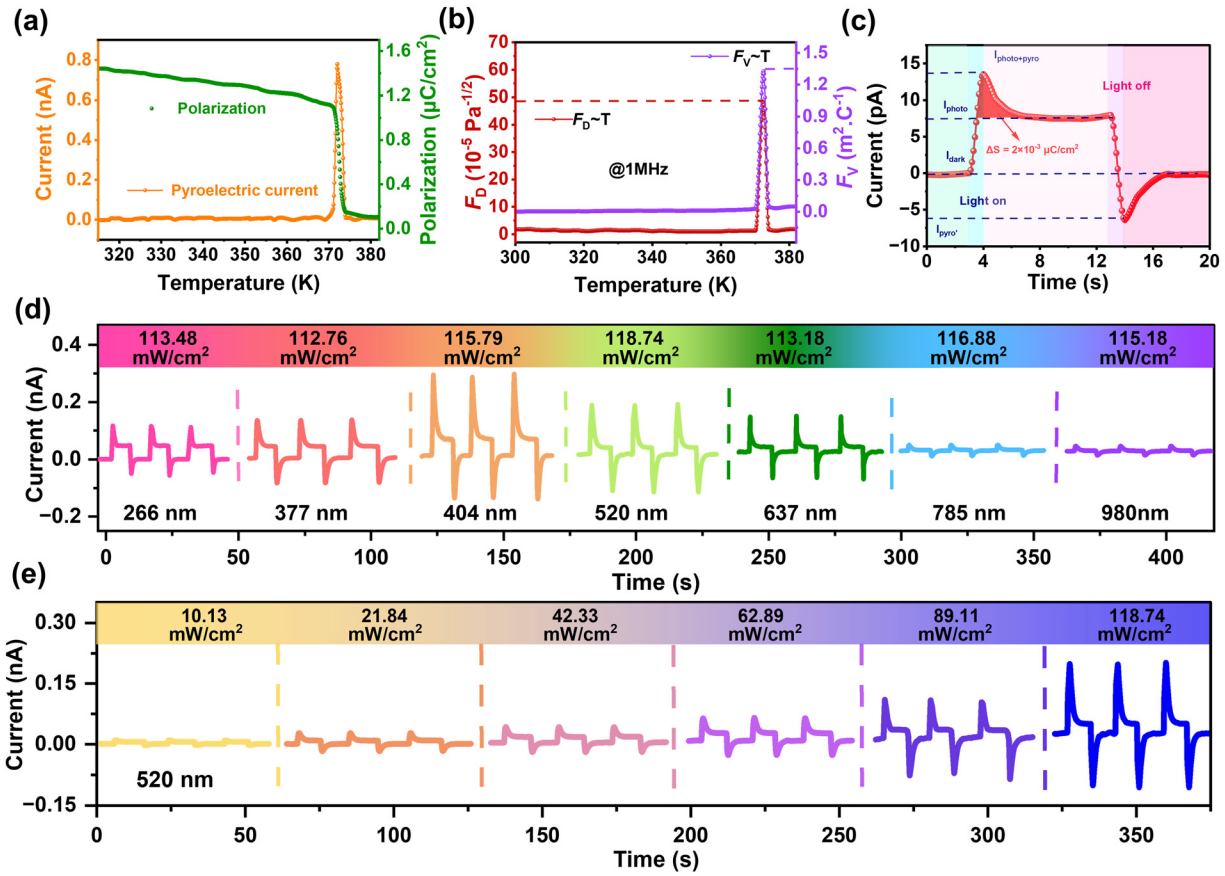

Fig. 4 (a) Temperature-dependent pyroelectric currents and P_s deduced by integrating pyroelectric current. (b) The simulated two FOMs of F_V and F_D. (c) I–t curves measured under 404 nm irradiation at zero bias (5.44 mW cm^{-2}). (d) Photoactivities of **1** under light illumination at different wavelengths. (e) I–t curves measured under 520 nm laser irradiation with different densities at zero bias.

Pyroelectric effect and broadband photoinduced response

Subsequently, we investigated the pyroelectric properties of **1** using single crystals, which demonstrate a sharp pyroelectric current arising from charge displacement near the T_c (Fig. 4a). The temperature dependence of polarization obtained through pyroelectric measurements gives a P_s value of approximately 1.4 μC cm^{-2}. As another important parameter, the pyroelectric coefficient (p_e, *i.e.*, $|\partial P_s/\partial T|$) is also estimated to be 2.5 × 10^{-3} μC cm^{-2} K^{-1} at room temperature, which increases to 0.64 μC cm^{-2} K^{-1} near the T_c (Fig. S6). The room-temperature value is smaller than those of conventional pyroelectric materials, such as triglycine sulfate (TGS, $p_e \approx 5.5 \times 10^{-2}$ μC cm^{-2} K^{-1}) and $Ba_{0.85}Ca_{0.15}Zr_{0.1}Ti_{0.9}O_3$ (BZT, $p_e \approx 9.8 \times 10^{-2}$ μC cm^{-2} K^{-1}).[50,51] For pyroelectric detection, two key pyroelectric FOMs are voltage responsivity $F_V = p_e/(\varepsilon_0\varepsilon_r c_v)$ and detectivity $F_D = p_e/[c_v(\varepsilon_0\varepsilon_r \tan\delta)^{1/2}]$, where ε_0 denotes the vacuum permittivity, c_v represents the volumetric heat capacity, and $\tan\delta$ is the dielectric loss. These FOMs quantify the maximum pyroelectric voltage per energy input and the weak-signal detection capability, respectively.[52] At room temperature, the F_V and F_D values of **1** are estimated as ~3.0 × 10^{-4} cm^2 μC^{-1} and ~1.24 × 10^{-5} Pa$^{-1/2}$, respectively. Owing to its improper ferroelectric, **1** exhibits significantly reduced ε_r and $\tan\delta$ values compared to proper ferroelectric counterparts. This results in a dramatic enhancement of the pyroelectric FOMs in the vicinity of the T_c (Fig. 4b).

To further study photosensitivity, light-induced pyroelectric measurements were performed at room temperature. Taking the 404 nm laser (5.44 mW cm^{-2}) as an example, the abrupt temperature increase at the crystal surface upon illumination reduces the polarization. This process disrupts the initial alignment of electric dipoles and generates a positive pyroelectric current. Under continuous illumination, the stabilization of temperature correlates with a steady photovoltaic current plateau. Upon light termination, the sudden surface cooling induces polarization variation that produces a transient pyroelectric current with the opposite direction, which rapidly decays to the dark state during prolonged darkness (Fig. 4c). Thermal equilibrium analysis reveals an integrated charge of 2 × 10^{-3} μC cm^{-2} over the temperature-rise fluctuation (red region, Fig. 4c and S7), yielding a p_e value of 2.33 × 10^{-3} μC cm^{-2} K^{-1} at this irradiance. This value coincides with that obtained from the pyroelectric measurement.

Fig. 4d displays light-induced pyroelectric currents measured along the polar *b*-axis at different wavelengths. For

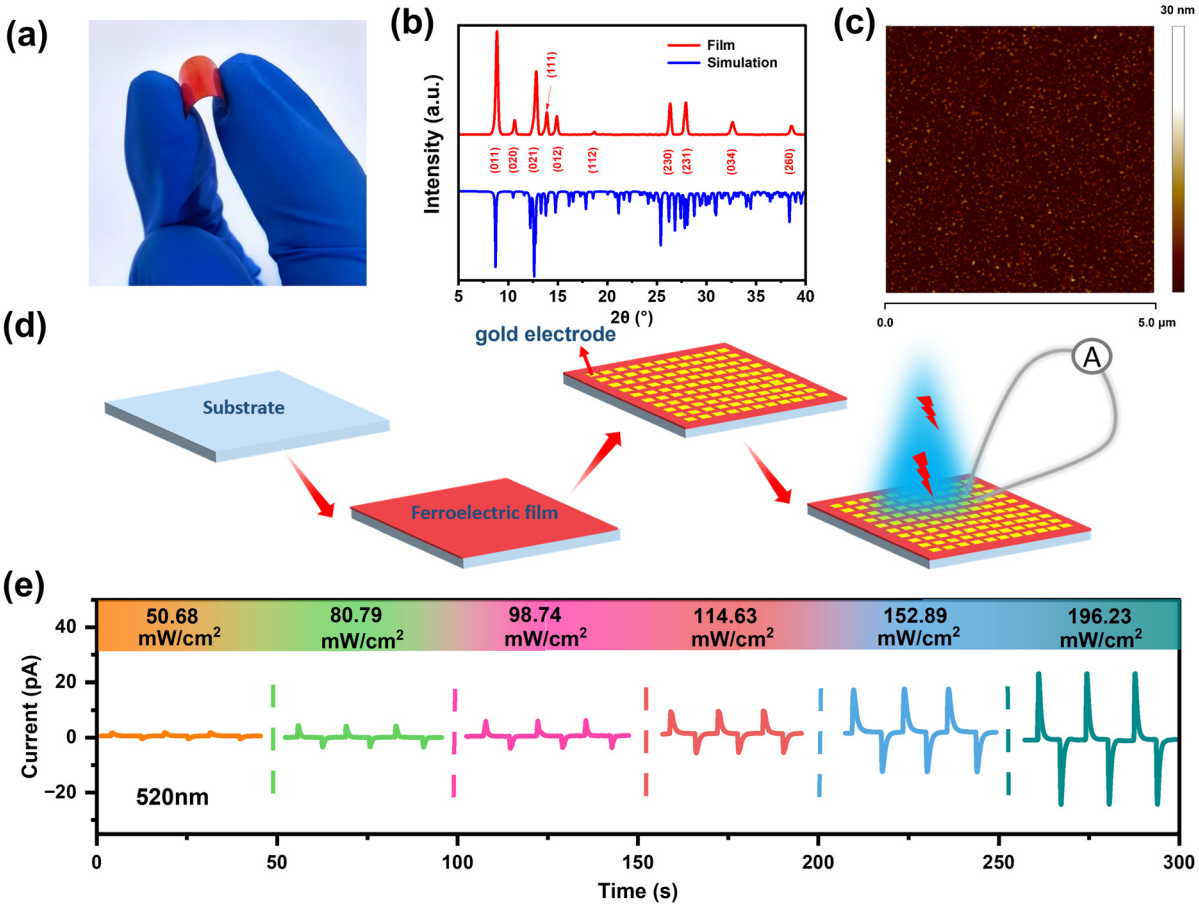

Fig. 5 (a) Image of the flexible ferroelectric film of **1**. (b) XRD patterns of the ferroelectric film based on the substrate platform and theoretical data. (c) AFM image of the thin film of **1**. (d) Schematic diagram of the thin-film device fabrication process. (e) *I*–*t* curves measured under 520 nm laser irradiation with different densities at zero bias.

incident light with wavelengths below the bandgap (266–637 nm), the transient pyroelectric current (I_{pyro}) and the steady photovoltaic current (I_{photo}) coexist. This coupling exhibits strong wavelength dependence, with maximum output emerging near 404 nm. Under above-bandgap wavelength irradiation, the attenuated I_{photo} nearly vanishes at photon energies far below the bandgap since low-energy photons cannot directly enhance charge carrier migration in **1**. However, distinct transient I_{pyro} peaks persist across a broad ultraviolet-to-infrared spectral range (up to 980 nm). The measured currents at fixed radiation intensity exhibit wavelength-dependent characteristics, which gradually decrease with increasing wavelength. Fig. 4e shows the corresponding current–time (*I*–*t*) curves under 520 nm laser irradiation at zero bias. With increasing incident power, the I_{pyro} peaks intensify significantly and demonstrate intensity-dependent behaviors. These results confirm that the coupling of photovoltaic I_{photo} and light-induced I_{pyro} would enhance photoresponsivity. In addition, photostability measurement at 404 nm (115.79 mW cm^{-2}) shows stable transient photopyroelectric outputs over multiple cycles without degradation (Fig. S8). Crystalline devices retain approximately 100% of their initial performance after two-months of ambient exposure (115.79 mW cm^{-2}, Fig. S9), demonstrating exceptional stability for practical application. Critically, all properties of **1** are achieved without external power (at zero bias), which establishes these polarization-directed characteristics as a promising platform for broadband photoactivity, particularly in self-powered photodetection.

Thin film characterization and photoinduced pyroelectric effects

Another striking feature is that **1** can be easily deposited on flexible plastic substrates *via* spin-coating. The films exhibit uniform red transparent surfaces (Fig. 5a) devoid of visible pinholes, indicative of high crystallite distribution. The scanning electron microscopy (SEM) image also confirms this conclusion (Fig. S10). The structure of the thin film is verified by XRD measurements, which shows good crystallinity and phase purity (Fig. 5b). Fig. 5c presents the height topography image of the ferroelectric thin film acquired using atomic force microscopy (AFM). AFM analysis reveals that the spin-coated film exhibits complete substrate coverage and exceptional surface uniformity, demonstrating nanoscale flatness with a

root mean square roughness of 3.68 nm. Profilometry measurements reveal a film thickness of 107.05 nm and a surface roughness of 3.92 nm (Fig. S11). This corroborates the superior film continuity, where the ultra-low defect density enables efficient charge transport and rapid response kinetics.[53] Furthermore, thin film devices were fabricated by sputtering gold electrodes on the surface of high-quality thin films (Fig. 5d). As shown in Fig. 5e, under zero bias and 520 nm laser illumination, the characteristic four-stage photoresponse behavior of the current over time is clearly observed, where the peak photocurrent gradually increases with higher incident light intensities. The consistency in response between thin-film and single-crystalline devices highlights the light-induced pyroelectric properties of **1** across different morphologies.

Conclusion

In summary, we have reported a molecular ferroelectric material, (DMAPA)BiI_5, that combines a narrow bandgap (1.94 eV) with excellent ferroelectricity. Furthermore, the improper ferroelectric nature of **1** endows it with a large pyroelectric FOM with the F_V and F_D peaks far exceeding those of conventional ferroelectric materials. Critically, **1** not only achieves broadband (266–980 nm) self-powered photoactivities in single-crystalline form but also demonstrates exceptional light-induced pyroelectric effects in thin-film devices. This study marks a critical step forward for molecular ferroelectrics, overcoming long-standing material morphology limitations while opening new avenues for autonomous optoelectronic device engineering.

Author contributions

Jialu Chen wrote the manuscript; Liwei Tang and Chen Gong performed the data analysis; Linjie Wei and Jingtian Zhang performed the validation; Xingguuang Chen and Xiaoyu Zhang performed the data curation; Yi Liu performed the methodology; Junhua Luo and Zhihua Sun reviewed this article.

Conflicts of interest

The authors declare no conflicts of interest.

Data availability

The data that support the findings of this study are available on request from the corresponding author.

Supplementary information (SI) is available. See DOI: **https://doi.org/10.1039/d5qi01797a**.

CCDC 2471887 and 2471892 contain the supplementary crystallographic data for this paper.[54a,b]

Acknowledgements

This work was supported by NSFC (22125110, U23A2094, 22205233, 22305248 and U21A2069), the Natural Science Foundation of Fujian Province (2023J02028 and 2025J01247), the Fujian Science & Technology Innovation Laboratory for Optoelectronic Information of China (2021ZR126), the Postdoctoral Fellowship Program of CPSF (GZB20240746), and the China Postdoctoral Science Foundation (2024T170923 and 2024M753233).

References

1 P.-P. Shi, Y.-Y. Tang, P.-F. Li, W.-Q. Liao, Z.-X. Wang, Q. Ye and R.-G. Xiong, Symmetry breaking in molecular ferroelectrics, *Chem. Soc. Rev.*, 2016, **45**(14), 3811–3827.
2 J. Liu, L. Su, X. Zhang, D. V. Shtansky and X. Fang, Ferroelectric–optoelectronic hybrid system for photodetection, *Small Methods*, 2024, **8**(2), 2300319.
3 P. Gao, C. T. Nelson, J. R. Jokisaari, S.-H. Baek, C. W. Bark, Y. Zhang, E. Wang, D. G. Schlom, C.-B. Eom and X. Pan, Revealing the role of defects in ferroelectric switching with atomic resolution, *Nat. Commun.*, 2011, **2**(1), 591.
4 W. Li, Y. Ma, Y. Liu, Q. Fan, H. Xu, W. Guo, L. Tang, H. Rong, Z. Sun and J. Luo, Zipper-like dynamic switching of coordination bonds gives a polar bimetallic halide toward self-driven X-ray detection, *Angew. Chem., Int. Ed.*, 2025, **64**(4), e202417036.
5 W.-J. Xu, S. Kopyl, A. Kholkin and J. Rocha, Hybrid organic–inorganic perovskites: Polar properties and applications, *Coord. Chem. Rev.*, 2019, **387**, 398–414.
6 C. Paillard, X. Bai, I. C. Infante, M. Guennou, G. Geneste, M. Alexe, J. Kreisel and B. Dkhil, Photovoltaics with ferroelectrics: Current status and beyond, *Adv. Mater.*, 2016, **28**(26), 5153–5168.
7 I.-H. Park, K. C. Kwon, Z. Zhu, X. Wu, R. Li, Q.-H. Xu and K. P. Loh, Self-powered photodetector using two-dimensional ferroelectric Dion–Jacobson hybrid perovskites, *J. Am. Chem. Soc.*, 2020, **142**(43), 18592–18598.
8 V. Dvořák, Improper ferroelectrics, *Ferroelectrics*, 1974, **7**(1), 1–9.
9 N. A. Benedek and C. J. Fennie, Hybrid improper ferroelectricity: A mechanism for controllable polarization–magnetization coupling, *Phys. Rev. Lett.*, 2011, **106**(10), 107204.
10 Z. Sun, Y. Tang, S. Zhang, C. Ji, T. Chen and J. Luo, Ultrahigh pyroelectric figures of merit associated with distinct bistable dielectric phase transition in a new molecular compound: Di-*n*-butylaminium trifluoroacetate, *Adv. Mater.*, 2015, **27**(32), 4795–4801.
11 L. Guo, X. Liu, L. Gao, X. Wang, L. Zhao, W. Zhang, S. Wang, C. Pan and Z. Yang, Ferro-pyro-phototronic effect in monocrystalline 2D ferroelectric perovskite for high-sensitive, self-powered, and stable ultraviolet photodetector, *ACS Nano*, 2022, **16**(1), 1280–1290.

12 Y. Ma, J. Wang, W. Guo, S. Han, J. Xu, Y. Liu, L. Lu, Z. Xie, J. Luo and Z. Sun, The first improper ferroelectric of 2D multilayered hybrid perovskite enabling strong tunable polarization-directed second harmonic generation effect, *Adv. Funct. Mater.*, 2021, **31**(37), 2103012.
13 L. Hua, J. Wang, Y. Liu, W. Guo, Y. Ma, H. Xu, S. Han, J. Luo and Z. Sun, Improper high-T_c perovskite ferroelectric with dielectric bistability enables broadband ultraviolet-to-infrared photopyroelectric effects, *Adv. Sci.*, 2023, **10**(19), 2301064.
14 J. F. Scott, Applications of modern ferroelectrics, *Science*, 2007, **315**(5814), 954–959.
15 R. Nechache, C. Harnagea, S. Li, L. Cardenas, W. Huang, J. Chakrabartty and F. Rosei, Bandgap tuning of multiferroic oxide solar cells, *Nat. Photonics*, 2015, **9**(1), 61–67.
16 H. Zhang, Z. Wei, P. Li, Y. Tang, W. Liao, H. Ye, H. Cai and R. Xiong, The narrowest band gap ever observed in molecular ferroelectrics: Hexane-1,6-diammonium pentaiodobismuth(III), *Angew. Chem., Int. Ed.*, 2018, **57**(2), 526–530.
17 Y. Shen, C. Ran, X. Dong, Z. Wu and W. Huang, Dimensionality engineering of organic–inorganic halide perovskites for next-generation X–ray detector, *Small*, 2024, **20**(16), 2308242.
18 M. Liu, H. Zhang, D. Gedamu, P. Fourmont, H. Rekola, A. Hiltunen, S. G. Cloutier, R. Nechache, A. Priimagi and P. Vivo, Halide perovskite nanocrystals for next-generation optoelectronics, *Small*, 2019, **15**(28), 1900801.
19 Y. Liu, Research progress on structure and property of hybrid organic–inorganic perovskite, *IOP Conf. Ser.: Earth Environ. Sci.*, 2021, **781**(2), 022069.
20 Y. Gao, E. Shi, S. Deng, S. B. Shiring, J. M. Snaider, C. Liang, B. Yuan, R. Song, S. M. Janke, A. Liebman-Peláez, P. Yoo, M. Zeller, B. W. Boudouris, P. Liao, C. Zhu, V. Blum, Y. Yu, B. M. Savoie, L. Huang and L. Dou, Molecular engineering of organic–inorganic hybrid perovskites quantum wells, *Nat. Chem.*, 2019, **11**(12), 1151–1157.
21 Z. Deng, J. Ma, Y. Peng, Y. Yao, Y. Chang, N. Qin, J. Jia, R. He, L. Zhou and M. Li, Embedding Te(IV) into a robust Sn(IV)-based metal halide for deep-red emission, *Inorg. Chem.*, 2025, **64**(8), 4103–4112.
22 Q. Li, S. Li, K. Wang, Z. Quan, Y. Meng and B. Zou, High-pressure study of perovskite-like organometal halide: Band-gap narrowing and structural evolution of $[NH_3\text{-}(CH_2)_4\text{-}NH_3]CuCl_4$, *J. Phys. Chem. Lett.*, 2017, **8**(2), 500–506.
23 C. Lin, Y. Zhao, Y. Liu, W. Zhang, C. Shao and Z. Yang, The bandgap regulation and optical properties of alloyed Cs^2NaSbX^6 (X = Cl, Br, I) systems with first principle method, *J. Mater. Res. Technol.*, 2021, **11**, 1645–1653.
24 A. H. Slavney, L. Leppert, A. Saldivar-Valdes, D. Bartesaghi, T. J. Savenije, J. B. Neaton and H. I. Karunadasa, Small-band-gap halide double perovskites, *Angew. Chem., Int. Ed.*, 2018, **57**(39), 12765–12770.
25 M. P. Hautzinger, W. Mihalyi-Koch and S. Jin, A-site, cation chemistry in halide perovskites, *Chem. Mater.*, 2024, **36**(21), 10408–10420.
26 F. Wu, X. Li, D. Pan, Z. Sun, J. Luo and X. Liu, Geometrical designing of a soft-layered halide perovskite improper photoferroelectric for boosted photostriction, *Adv. Opt. Mater.*, 2023, **11**(23), 2300967.
27 X. Chen, M. Jia, W. Xu, G. Pan, J. Zhu, Y. Tian, D. Wu, X. Li and Z. Shi, Recent progress and challenges of bismuth-based halide perovskites for emerging optoelectronic applications, *Adv. Opt. Mater.*, 2023, **11**(3), 2202153.
28 Z. Sun, A. Zeb, S. Liu, C. Ji, T. Khan, L. Li, M. Hong and J. Luo, Exploring a lead-free semiconducting hybrid ferroelectric with a zero-dimensional perovskite-like structure, *Angew. Chem.*, 2016, **128**(39), 12033–12037.
29 T. Zhu, Y. Yang and X. Gong, Recent advancements and challenges for low-toxicity perovskite materials, *ACS Appl. Mater. Interfaces*, 2020, **12**(24), 26776–26811.
30 C.-D. Liu, C.-C. Fan, B.-D. Liang, C.-Y. Chai, C.-Q. Jing, X.-B. Han and W. Zhang, Spectrally selective polarization-sensitive photodetection based on a 1D lead-free hybrid perovskite ferroelectric, *ACS Mater. Lett.*, 2023, **5**(7), 1974–1981.
31 W. Li, D. Xin, S. Tie, J. Ren, S. Dong, L. Lei, X. Zheng, Y. Zhao and W.-H. Zhang, Zero-dimensional lead-free $FA_3Bi_2I_9$ single crystals for high-performance X-ray detection, *J. Phys. Chem. Lett.*, 2021, **12**(7), 1778–1785.
32 M. Chen, X. Dong, D. Chu, B. Jia, X. Zhang, Z. Zhao, J. Hao, Y. Zhang, J. Feng, X. Ren, Y. Liang, R. Shi, A. Najar, Y. Liu and S. Liu, Interlayer-spacing engineering of lead-free perovskite single crystal for high-performance X-ray imaging, *Adv. Mater.*, 2023, **35**(18), 2211977.
33 Y. Liu, Z. Xu, Z. Yang, Y. Zhang, J. Cui, Y. He, H. Ye, K. Zhao, H. Sun, R. Lu, M. Liu, M. G. Kanatzidis and S. Liu, Inch-size 0D-structured lead-free perovskite single crystals for highly sensitive stable X-ray imaging, *Matter*, 2020, **3**(1), 180–196.
34 S. Tie, W. Zhao, D. Xin, M. Zhang, J. Long, Q. Chen, X. Zheng, J. Zhu and W. Zhang, Robust fabrication of hybrid lead-free perovskite pellets for stable X-ray detectors with low detection limit, *Adv. Mater.*, 2020, **32**(31), 2001981.
35 X. Chen, M. Jia, W. Xu, G. Pan, J. Zhu, Y. Tian, D. Wu, X. Li and Z. Shi, Recent progress and challenges of bismuth-based halide perovskites for emerging optoelectronic applications, *Adv. Opt. Mater.*, 2023, **11**(3), 2202153.
36 Z. Xiao, W. Meng, J. Wang and Y. Yan, Thermodynamic stability and defect chemistry of bismuth-based lead-free double perovskites, *ChemSusChem*, 2016, **9**(18), 2628–2633.
37 M. Leng, Y. Yang, K. Zeng, Z. Chen, Z. Tan, S. Li, J. Li, B. Xu, D. Li, M. P. Hautzinger, Y. Fu, T. Zhai, L. Xu, G. Niu, S. Jin and J. Tang, All-inorganic bismuth-based perovskite quantum dots with bright blue photoluminescence and excellent stability, *Adv. Funct. Mater.*, 2018, **28**(1), 1704446.
38 W. Guo, H. Xu, W. Weng, L. Tang, Y. Ma, Y. Liu, L. Hua, B. Wang, J. Luo and Z. Sun, Broadband photoresponses from ultraviolet to near-infrared (II) region through light-induced pyroelectric effects in a hybrid perovskite, *Angew. Chem., Int. Ed.*, 2022, **61**(52), e202213477.
39 L. Tang, S. Han, Y. Ma, Y. Liu, L. Hua, H. Xu, W. Guo, B. Wang, Z. Sun and J. Luo, Giant near-room-temperature

pyroelectric figures-of-merit originating from unusual dielectric bistability of two-dimensional perovskite ferroelectric crystals, *Chem. Mater.*, 2022, **34**(19), 8898–8904.

40 H. Ye, Y. Peng, X. Shang, L. Li, Y. Yao, X. Zhang, T. Zhu, X. Liu, X. Chen and J. Luo, Self-powered visible-infrared polarization photodetection driven by ferroelectric photovoltaic effect in a Dion–Jacobson hybrid perovskite, *Adv. Funct. Mater.*, 2022, **32**(24), 2200223.

41 A. V. Bune, V. M. Fridkin, S. Ducharme, L. M. Blinov, S. P. Palto, A. V. Sorokin, S. G. Yudin and A. Zlatkin, Two-dimensional ferroelectric films, *Nature*, 1998, **391**(6670), 874–877.

42 G. H. Haertling, Ferroelectric ceramics: History and technology, *J. Am. Ceram. Soc.*, 1999, **82**(4), 797–818.

43 S. R. Basu, L. W. Martin, Y. H. Chu, M. Gajek, R. Ramesh, R. C. Rai, X. Xu and J. L. Musfeldt, Photoconductivity in $BiFeO_3$ thin films, *Appl. Phys. Lett.*, 2008, **92**(9), 091905.

44 H. Ye, W. Liao, C. Hu, Y. Zhang, Y. You, J. Mao, P. Li and R. Xiong, Bandgap engineering of lead–halide perovskite-type ferroelectrics, *Adv. Mater.*, 2016, **28**(13), 2579–2586.

45 W.-Q. Liao, Y. Zhang, C.-L. Hu, J.-G. Mao, H.-Y. Ye, P.-F. Li, S. D. Huang and R.-G. Xiong, A lead-halide perovskite molecular ferroelectric semiconductor, *Nat. Commun.*, 2015, **6**(1), 7338.

46 Z. Sun, A. Zeb, S. Liu, C. Ji, T. Khan, L. Li, M. Hong and J. Luo, Exploring a lead-free semiconducting hybrid ferroelectric with a zero-dimensional perovskite-like structure, *Angew. Chem.*, 2016, **128**(39), 12033–12037.

47 R.-G. Xiong, D.-W. Fu and Y. Zhang, Applications of Curie symmetry principle in molecular ferroelectrics, *Acta Crystallogr., Sect. A:Found. Adv.*, 2017, **73**(a2), C33–C33.

48 K. Suzuki and K. Kijima, Optical band gap of barium titanate nanoparticles prepared by RF-plasma chemical vapor deposition, *Jpn. J. Appl. Phys.*, 2005, **44**(4R), 2081.

49 L. Wang, F. Zhang, C. Chen, X. He, M. A. Boda, K. Yao and Z. Yi, Bandgap engineering of BZT-BCT by Mn doping and the emerging strong photo-pyroelectric effect, *Nano Energy*, 2024, **119**, 109081.

50 P. Felix, P. Gamot, P. Lacheau and Y. Raverdy, Pyroelectric, dielectric and thermal properties of TGS, DTGS and TGFB, *Ferroelectrics*, 1977, **17**(1), 543–551.

51 M. Sharma, V. P. Singh, S. Singh, P. Azad, B. Ilahi and N. A. Madhar, Porous $Ba_{0.85}Ca_{0.15}Zr_{0.1}Ti_{0.9}O_3$ ceramics for pyroelectric applications, *J. Electron. Mater.*, 2018, **47**(8), 4882–4891.

52 H. Estrada-Vazquez, R. T. Webster and P. Das, Transverse-acoustoelectric-voltage (TAV) spectroscopy of high-resistivity GaAs, *J. Appl. Phys.*, 1979, **50**(7), 4913–4919.

53 C. Zhao, X. Lai, D. Liu, X. Guo, J. Tian, Z. Dong, S. Luo, D. Zhou, L. Jiang, R. Huang and M. He, Molecular-dipole oriented universal growth of conjugated polymers into semiconducting single-crystal thin films, *Nat. Commun.*, 2025, **16**(1), 1509.

54 (*a*) CCDC 2471887: Experimental Crystal Structure Determination, 2025, DOI: **10.5517/ccdc.csd.cc2nz695**; (*b*) CCDC 2471892: Experimental Crystal Structure Determination, 2025, DOI: **10.5517/ccdc.csd.cc2nz6gb**.